Evidence and importance of intermediate nanostructures in the journey from molecular precursors to allophane and imogolite nanocrystals

Pierre Picot, Tobias Lange, Fabienne Testard, Frederic Gobeaux, Antoine Thill

Evidence and importance of intermediate nanostructures in the journey from molecular precursors to allophane and imogolite nanocrystals.

Pierre Picot[a],Tobias Lange[a,b],Fabienne Testard[a], Frederic Gobeaux[a] and Antoine Thill[a,*]

[a] Université Paris-Saclay, CEA, CNRS, NIMBE, 91191 Gif-sur-Yvette, France.
[b] CEA, DES, ISEC, DMRC, Univ. Montpellier, Marcoule, France.

April 25, 2023

Abstract

Nanoparticles often-called proto-imogolites have been identified as an intermediate in the formation process of imogolite nanotubes as early as 1979. Their composition and structure are now well documented in the case of synthetic imogolite. One specific characteristic of proto-imogolite is that they have a curved shape with a local structure close to the one of imogolite. During a growth stage, they evolve toward nanocrystals (allophane, imogolite), their thorough characterization has so far been difficult. Using synchrotron Small Angle X-ray Scattering coupled with Raman spectroscopy, we observe that proto-imogolites form during the initial stage of the co-precipitation of aluminum and silicon molecular precursors thanks to a reorganization process. The shape of the initial proto-imogolites, before the growth stage, depends on the synthesis conditions and controls the characteristics of the final product. We show using cryo-TEM images that, at the end of the growth stage, non-tubular nanostructures continue to coexist with nanotubes. Protocols to quantify remaining non-tubular nano-objects and purify the samples are discussed.

1 Introduction

The alteration of volcanic minerals and glasses in slightly acidic conditions leads to the formation of imogolite and allophane [1]. Imogolite is a tubular nanocrystal with a monodisperse diameter and a thin wall thickness of 5 Å. Its composition from the outside to the inside surface reads $(HO)_3Al_2O_3SiOH$. Allophane has a less well-defined composition with a Si/Al ratio ranging from 0.5 to 1. A common characteristic of allophane is to have a hollow spherical shape with a wall thickness of also about 5 Å. In slightly acidic environments, Al and Si cations released from the primary minerals (quartz, feldspar, plagioclase, muscovite, biotite, amphibole, pyroxene...) alteration form spontaneously hydroxyaluminosilicate (HAS) that have a very low solubility [2, 3]. It has been proposed to classify these resulting products into two types by their local structure, called HAS_A and HAS_B, depending on the concentration and ratio between Al and Si [3]. For $Si/Al < 1$ mainly HAS_A precipitates. Filterable HAS_A solids are dominated by silicon coordinated through three $Si-O-Al$ bonds ($Q_0(3Al)$). Such coordination is typical of the so-called Imogolite Local Structure (ILS). Its very specific narrow ^{29}Si NMR signal at -79 ppm has been used to identify imogolite in soils [4]. HAS_A compounds do not necessarily have the exact same local-structure as imogolite or allophane but we can hypothesize that HAS_A precipitates can lead to an ILS through internal reorganization [5, 6]. Indeed, HAS_A contains only octahedric coordinated aluminum Al^{VI} associated with tetrahedric Si^{IV} with the same Si/Al ratio as imogolite. The most thermodynamically stable structure for the smallest HAS_A polycation consists of two Al^{VI} octahedra that are edge bonded by two $Al-\mu_2OH$ bonds and a Si^{IV} tetrahedron with two $Si-O-Al$ bonds [7]. The identification of nanostructured precipitates as an intermediate stage of imogolite formation has been very early recognized and the term proto-imogolite was used to describe them. For example, based on IR and diffraction data, Farmer et *al.* said in 1979 "Similarly, proto-imogolite can be presumed to incorporate orthosilicate groups attached to fragments of gibbsite-like sheets of aluminum hydroxides" [8].
Proto-imogolite intermediates in the precipitation of aluminosilicate have not been the subject of many publications [9]. The low concentration of most of the standard imogolite synthesis protocols, their very small size and their high reactivity probably hinder their thorough characterization. Mukherjee et *al.* [10] and later Levard et *al.* [11] have studied the formation of germanium based imogolite nanotubes and both observed that initial nanometric objects are also involved in the growth process. Mukherjee et *al.* initially considered these nanostructures as amorphous nanoparticles. Later, it has been recognized that, as for silicon-based imogolite, they already share the same local structure as the final nanotubes. Levard et *al.* demonstrated that the synthesis of germanium based imogolite is possible even at high concentration with a few days of growth [12]. Based on the results of

a combination of techniques (ICP, EXAFS, DLS, SAXS and cryo-TEM), they proposed a tile-like nanostructure that has the same local structure as the final nanotubes with a size of about 5 nm [11]. Thill et *al*. showed the first cryo-TEM images of the proto-imogolite which tend to confirm such a tile-shape [6, 13]. Yucelen et *al*. have studied the shape and the role of proto-imogolite in the formation of imogolite nanotubes of various diameters using a combination of NMR and ESI-MS techniques [5]. They demonstrate that anions are coordinated to hydroxyaluminosilicate curved polycations. DFT calculations on such tile-shaped nanostructures revealed that the type of anion attached to proto-imogolite modifies their curvature. Furthermore, they suggested that the type of acid used in the precipitation of imogolite nanotubes from aluminum and silicon alkoxide precursors controls the diameter of the final nanotubes in the same way as the curvature of proto-imogolite [14]. This seems to be in favor of the self-assembly process of the imogolite nanotubes already hypothesized by Thill and Yucelen in imogolite growth kinetics models [15, 16].

The formation of imogolite from proto-imogolite is considered a nucleation event [17, 18, 19]. It is generally performed at elevated temperature for several days. However, the origin and characteristics of the energy barrier associated with the nucleation event from proto-imogolite to imogolite or allophane have never been discussed to our knowledge. Using adsorption on mica surfaces at different stages of the synthesis process, Du et *al*. were able to observe the transition from proto-imogolite to allophane and imogolite [20]. At a very early stage, the mica surface is covered with a layer of nanoparticles with a height of less than one nanometer. It has been interpreted as proto-imogolites adsorbed flat on the mica surface. Allophanes are observed in the initial growth stage as spherical objects with a height of more than 4 nm. Finally, nanotubes are observed with a typical elongated shape and height of 2 nm. The term open-ILS is introduced to refer to proto-imogolite before the growth stage. This notation is well suited to describe the tile shape of proto-imogolite being too small to close in the form of a nanotube or a nanosphere. In this line of thought, allophane and imogolite would be closed-ILSs that result from the assembly of several open-ILSs or their growth until they are large enough to close. The nucleation barrier can be hypothesized to occur in the transition from open-ILS to closed-ILS. It is reasonable to think that such a nucleation event can lead to several nanocrystal polymorphs which are allophanes (sphere), imogolites (nanotube) of various chiralities or less well-defined closed-ILS nanostructures or aggregates [13, 20, 21, 22].

Upon successful synthesis, imogolite is obtained in the form of very well dispersed perfectly transparent suspensions. Any turbidity would be due to the formation of large crystals of aluminum hydroxides (Gibbsite or Boehmite). These transparent dispersions however still contain non-tubular objects in various proportions.

Generally, imogolites are recovered by centrifugation after adding a concentrated salt solution or after increasing the pH [17]. The result of this pH adjustment or addition of salt is the formation of nanotube bundles and aggregates that are then easily separated from water by centrifugation in the form of a concentrated gel. The relative height of the gel in the centrifuge tube in standard conditions was used by Farmer to compare the imogolite yield of different synthesis routes [17], even though non-tubular nanostructures also take part in the formation of this gel. After separation, the gel is then redispersed with an acid and eventually dialyzed. The drawback of this method is that the aggregation/gelation steps lead to the formation of imogolite bundles that is not totally reversible. In addition, the effect of these steps on other closed-ILS nanostructures is not benign. Indeed, to eliminate the small non-tubular particles, some authors use chemical attack steps. It is known that acidification and other chemical digestion procedures are effective to get rid of non-tubular poorly crystallized products [23]. Therefore, authors using an acid redispersion stage of the gel are, at least in part, getting rid of some of the smallest non-tubular nanoparticles. When the proportion of non-tubular nanoparticles is huge, such a chemical purification step is very effective to retrieve nanotubes [24, 25]. However, nothing can be inferred on the proportion and on the role of small closed-ILS nanostructures when such purification techniques have been used.

Concentration procedures may be designed to preserve the nanotube dispersion state. For example, imogolite can be retrieved by filtration with a very small membrane cutoff (i.e. 8 – 10 kD) [13] or by evaporation [26]. In these cases, nanotubes and co-existing non-tubular products like allophane or other less well-defined closed-ILS nanostructures are also concentrated without compromising their stability. As no precipitation or acidic redispersion steps are required, resulting products contain well-dispersed nanotubes, but they can also contain a high amount of non-tubular closed-ILS. For such preserved samples, it is very difficult to assess the quantity or even the presence of non-tubular closed-ILS. Measurements by SAXS and IR spectroscopy cannot indicate the presence of non-tubular closed-ILS when their mass fraction is reduced to a few percent. However, at such low mass fraction, cryo-TEM can qualitatively reveal their presence in coexistence with very long nanotubes [14, 26, 27]. When non-tubular closed-ILSs occur in high proportion, SAXS curves are deformed and their IR spectrum is modified [17]. Knowing if these non-tubular closed-ILSs remaining after the growth stage are initial non reacted open-ILSs, allophanes or other types of non-tubular closed-ILSs is not yet resolved. Their characterization and quantification are very delicate [17] even more because, as mentioned previously, the various protocols applied to retrieve the nanotubes may modify their proportion, sometimes intentionally. Recently, it was demonstrated that a size threshold exists in open-ILS for which the

curvature changes from sphere-like to tube-like [28]. It is therefore important to characterize open-ILS nanostructures before the growth stage especially to compare their average size with the sphere-tube transition threshold. In this article, we illustrate the presence of remaining non-tubular nanostructures (closed-ILS) at the end of the growth stage for several samples by Cryo-TEM and ultrafiltration methods. To better understand their origin and role, we have explored the early stages of precipitation of Al and Si at different concentrations (millimolar and centimolar) and different NaOH injection speeds (fast and slow). Small Angle X-ray Scattering at the SWING beamline of synchrotron Soleil and Raman spectroscopy were used to continuously monitor the co-precipitation of Al and Si for several hours. After a growth stage at 90°C for 5 days, the dispersions were characterized by IR spectroscopy and laboratory SAXS experiments in order to assess the impact of the open-ILS structure on the final morphologies and proportions of closed-ILS.

2 Experimental

2.1 Cryo-TEM

Cryo-TEM observations of various typical samples were conducted at low temperature (-180 °C) on a JEOL 2010 FEG microscope operated at 200 kV. Images were recorded with a Gatan camera. A drop of the solution was deposited on a copper grid covered with a holey carbon film (Quantifoil R2/2) that was previously treated by a plasma glow discharge. Excess liquid on the grid was blotted out with filter paper and the grid was quickly plunged in liquid ethane to form a thin vitreous ice film. The whole process was performed using a Vitrobot apparatus (FEI Company).

2.2 Synthesis for synchrotron experiments

Chemicals were purchased from Sigma-Aldrich and used as received. The protocol was adapted for synchrotron SAXS monitoring from the one described by Farmer et *al.*[27] The predefined volume of tetraethoxysilane (TEOS) needed to reach a Si/Al ratio of 0.55 was stored in a syringe connected to a first syringe pump. On a second syringe pump, the required volume of NaOH solution was prepared to be able to reach a OH/Al ratio of 2. A remote signal sent to the syringe pumps triggered the injection of these volumes to be fed into a 50 mL stirred solution of $Al(ClO_4)_3$. The first pump injects the TEOS at $50\,mL{\cdot}min^{-1}$. The second pump is programmed to inject 25 mL of NaOH at $50\ mL{\cdot}min^{-1}$ (fast injection) or $0.1\,mL{\cdot}min^{-1}$ (slow injection). The concentration of aluminum and silicon precursors, start of add time for TEOS and NaOH solutions and injection flowrate for the different syntheses

are reported in Table 1. A peristaltic pump circulates the sample in a capillary placed in the X-ray beam. In the synthesis reactor, a pH-meter is continuously monitoring the pH and an optical fiber is used to collect the RAMAN spectrum. At the end of the SAXS experiment, the suspension is collected. The SAXS signal is measured again after at least 10 hours. The solution is then kept for five days at 90°C in an oven. Afterward, an 8 – 10 kD membrane was used to concentrate the imogolite dispersion up to $10\,\mathrm{g{\cdot}L^{-1}}$ by ultra-filtration. The final products are measured on a laboratory SAXS apparatus.

2.3 Dialysis

Dialysis membranes with a molecular weight cut-off (MWCO) of 8 – 10 kD were purchased from Spectrumlabs. The membranes were soaked in deionized water for at least 30 min and abundantly rinsed before use. After filling them with the imogolite dispersion, they were closed with clips and immersed into deionized water. The water was renewed every 24 h for five days.

2.4 IR spectroscopy

An aliquot of the final products has been dried and KBr pellets were prepared by compressing approximately 1 mg of sample dispersed in 100 mg of KBr. FTIR spectra (200 scans) were collected in transmission from 4000 to $400\,\mathrm{cm^{-1}}$ with a resolution of $4\,\mathrm{cm^{-1}}$ (Vertex 70, Bruker). All spectra were treated using OPUS software and subtracted from KBr. The resulting curves were corrected using OPUS tools (water and CO_2 compensation, baseline correction).

2.5 Small Angle X-ray Scattering

Synchrotron SAXS experiments were conducted in air at the SWING line in SOLEIL Synchrotron equipped with an AVIEX170170 CDD detector, a monochromatic beam ($\lambda = 0.827$ Å) and a flux of 10^{12} photon·s^{-1}. The detector count was normalized by the direct beam and the calibration was verified with water. Standard procedures were applied using the Foxtrot software (version 3.3.4) to subtract background scattering and to normalize the intensities. For millimolar conditions, a measurement of one second is made every 30 seconds. For the centimolar condition, several loops of 255 measurements of one second are acquired with 0.5 s of dead time between measurements. Lab Small Angle X-ray Scattering (SAXS) experiments were acquired under vacuum with a Xeuss 2.0 apparatus (Xenocs) equipped with a Pilatus3 R 1M detector (Dectris). The intensity is plotted against the scattering vector $q = 4\pi \cdot sin(\theta) \cdot \lambda^{-1}$, with λ as the wavelength (0.1542 nm) and 2θ as the scattering angle. The sample-to-detector distance can be adjusted

(used distances were 42.3; 53.7; 119.4 cm) and was calibrated with tetradecanol. The detector count was normalized by the direct beam and the calibration was verified with Lupolen. Standard procedures were applied using the open-source pySAXS software to subtract background scattering and to normalize the intensities. Samples were sealed in glass capillaries (diameter 1.5 mm, wall thickness 0.1 mm, WJM-Glas) or in Kapton capillaries (diameter 1.506 mm, wall thickness 41.9 µm, MicroLumen). Each sample was measured for one hour.

2.6 Raman

Raman data are recorded using the RXN1-785 Raman spectrometer from Kaiser Optical Systems, Inc. (KOSI) equipped with a near-IR laser diode working at 785 nm as excitation light, and with a CCD detector for providing fast and simultaneous full spectral collection of Raman data from 50 to 3450 cm^{-1}. The laser excitation is obtained in the sample using a remote probe head. The probe head is equipped with an immersion optic with a long fixed focal length (3 mm). The transmitted laser power at the sample position is 50 mW. A second optical fiber is used for the collection of the scattered Raman signals. One spectrum is recorded every 60 s in the cycle mode available with the HoloReact software developed by KOSI. This spectrum corresponds to ten spectra recorded with an integration time of 1 s and averaged.

3 Results and Discussion

3.1 Evidence of open-ILS and closed-ILS nanostructures

Very few direct observations of open-ILS before heat treatment are available in the literature [13]. Only cryo-TEM observations enable the acquisition of unbiased images of non-tubular nano-objects during imogolite or allophane synthesis. Figure 1 shows several typical high-resolution cryo-TEM pictures of various samples. Figure 1A is the resulting suspension obtained after a growth stage at high temperature following a similar recipe as the one used by Du et *al.* for allophane synthesis [29]. In this sample, all nano-objects are non-tubular. They consist of a mixture of closed hollow spherules (allophane) and tile-like curved opened objects (open-ILS) isolated, aggregated or stacked. An electrostatic interaction exists between proto-imogolites due to the positively charged external (concave) surface and negatively charged internal (convex) surface [30]. A nice illustration of the existence of this attraction is obtained during the formation of Double-Walled nanotubes discovered by Maillet et *al.* in the case of germanium-based imogolite [13, 31]. This attraction is active only for open-ILS nanostructures. In this case, the internal

surface composed of $Si-OH$ groups is still accessible to the bulk solvent and interaction with other surfaces is still possible. Once closed-ILS are obtained in the form of a nanotube, a nanosphere or a less well-defined nanostructure, mainly the external (concave) surface is able to interact, and repulsive electrostatic interactions dominate. Figure 1B illustrates the morphology of nanostructures in

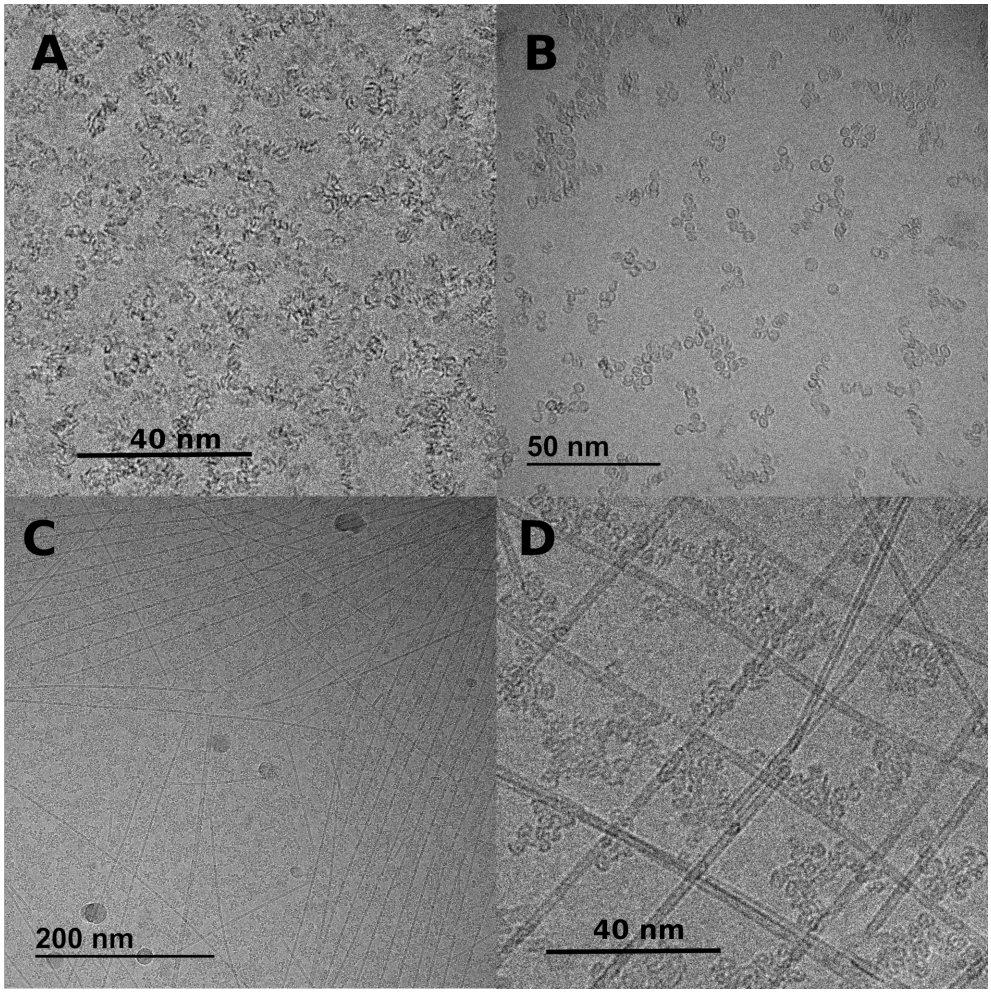

Figure 1: Cryo-TEM pictures of various products illustrating the shape of proto-imogolites and their coexistence with imogolite and allophane. A) and B) allophane syntheses C) and D) imogolite synthesis at different magnifications.

another allophane synthesis observed at a higher dilution. Some of the observed closed-ILSs have a very well-defined circular shape with a diameter of about 4 nm and could correspond to allophane. Others are less obviously completely closed or correspond to closed-ILSs with a less well-defined nanostructure. Figure 1C and D show high-resolution cryo-TEM images of a concentrated imogolite suspension.

The nanotubes have a diameter of about 2.4 nm. The nanotubes tend to have a parallel orientation. This is due to their strong electrostatic repulsion which, helps to trigger a liquid crystal organization at very low concentration [32]. In the space between the nanotubes, non-tubular nanostructures are observed, form aggregates between themselves and with the nanotubes. In Figure 1D, the structure of the non-tubular nanostructures is difficult to assess, but their shape and their interaction seem to correspond to closed-ILS. Finally, just by looking at various cryo-TEM pictures of final products obtained using ultrafiltration concentration and dialysis processes reveals that those non-tubular objects coexist with allophane or imogolite even at the end of the growth stage. This was already observed by Wada et *al.*, Koenderick et *al.* and more recently by Du et *al.* but cryo-TEM is providing an experimental insight of the presence of such nanostructures with minimal artifacts due to sample preparation [20, 23, 24]. We hypothesize that these non-tubular nanostructures are closed-ILS having a less well defined shape compared to allophane or imogolite. Their presence after a long lasting growth stage suggests that they that they are not able to evolve toward a tubular or spherical shape.

3.2 From molecular precursors to open-ILS

In order to better understand the formation kinetics of the proto-imogolites (open-ILS), we have followed the precipitation of molecular precursors in classical syntheses inspired by Farmer et *al.* [27] using a combination of Small Angle X-ray Scattering and Raman spectroscopy (see conditions in Table 1).

Table 1: Conditions of the SAXS experiments for initial co-precipitation of *Si* (from TEOS) and *Al* (from $Al(ClO_4)_3$). Q_{NaOH} is the flow rate of NaOH solution and times correspond to the beginning of addition.

Kinetic	*Al* (mM)	*Si* (mM)	Q_{NaOH} ($mL{\cdot}min^{-1}$)	T_{NaOH} (min)	T_{TEOS} (min)
1	2.9	1.6	0.1	10	15
2	3.3	1.8	50	10	10
3	27	15	50	10	5

Scattered intensities as a function of the scattering vector q for three kinetic experiments are presented in Figure 2 at different times. In all conditions, the scattered intensity increases during NaOH injection. HO^- triggers the replacement of aquo ligands in the first coordination shell of the Al^{3+} cations. This favors the formation of polycations through nucleophilic attack by HO^- ligands toward another Al^{3+} cation. The growth of polycations induces an increase of the scattered intensity. Unlike imogolite or allophane where the monodisperse character induces oscillations in the scattered intensity, at this stage no characteristic size

is noticeable. For kinetic 1, the scattered intensity displays a smooth q^{-2} trend that is typical of 2D objects. This is consistent with the expected scattering from tile shaped open-ILS [11]. In the case of kinetic 2, the scattered intensity has a higher slope at low angle. This can be the signature of a more three-dimensional structure. This trend is even more pronounced for kinetic 3.

The scattered intensity at the smallest angle is proportional to the average mass of the polycations. To discuss the evolution of this average mass, Figure 3 compares the scattered intensity at the smallest measured angle I_{qmin} normalized by the total concentration $C_{tot} = C_{Al} + C_{Si}$ for the three kinetic experiments. It is observed that for the slow injection rate of NaOH, the value of I_{qmin} increases linearly up to 260 minutes *i.e.* when NaOH injection ends. The increase in average mass seems thus to be directly controlled by the injected volume of NaOH. After the end of NaOH injection, the signal continues to be monitored and it displays a small decrease of the maximum intensity. For kinetic 1 a total of 5.8 mM has been injected at a constant rate of 0.1 mL·min^{-1}. During this injection period, the pH barely changed from 4.1 to 4.8 at the end of the NaOH injection (figure S1). Therefore, almost all HO^- are consumed to create $Al-OH-Al$ bonds, which drives the growth of the polycations. At the end of the injection, a slight decrease in size (and pH) is probably due to the hydrolysis of some $Al-OH-Al$ bonds releasing protons in the solution. For fast injection rates, I_{qmin} also increases during NaOH injection. For millimolar concentration (kinetic 2), pH increases slightly more than in the case of slow injection with a final pH of 5. In this case also, almost all the hydroxyls are consumed to trigger the growth of Al polycations. The evolution of I_{qmin} after the end of NaOH injection depends on concentration. For kinetic 2, I_{qmin} decreases during the whole measurement session. For kinetic 3, I_{qmin} quickly decreases and reaches a minimum value at about 38 minutes after the end of HO^- injection (purple curve in Figure 2). Then, I_{qmin} value increased very slowly while the pH continues to decrease.

It is interesting to note that the speed of injection matters to control the maximum size of aluminum polycations. Indeed, with slow injection I_{qmin}/C_{tot} reaches a maximum value of 0.007 cm^{-1}·L·mol^{-1} while for kinetic 2 it reaches a twice larger value of 0.014 cm^{-1}·L·mol^{-1}. As I_{qmin}/C_{tot} is proportional to the average mass of the polycations, this means that upon fast injection much larger structures are obtained initially and they go through a restructuration and size decrease. On the contrary, for kinetic 1 the final size is smaller which probably means that during the NaOH injection both growth and internal restructuration are active, which limits the final polycations size when the hydrolysis ratio reaches 2. It is interesting to compare the size decrease of the polycations for kinetics 2 and 3 (fast NaOH injection). For both conditions, the same I_{qmin}/C_{tot} is reached after NaOH injection, but the size decrease is much faster for kinetic 3 (high concentration).

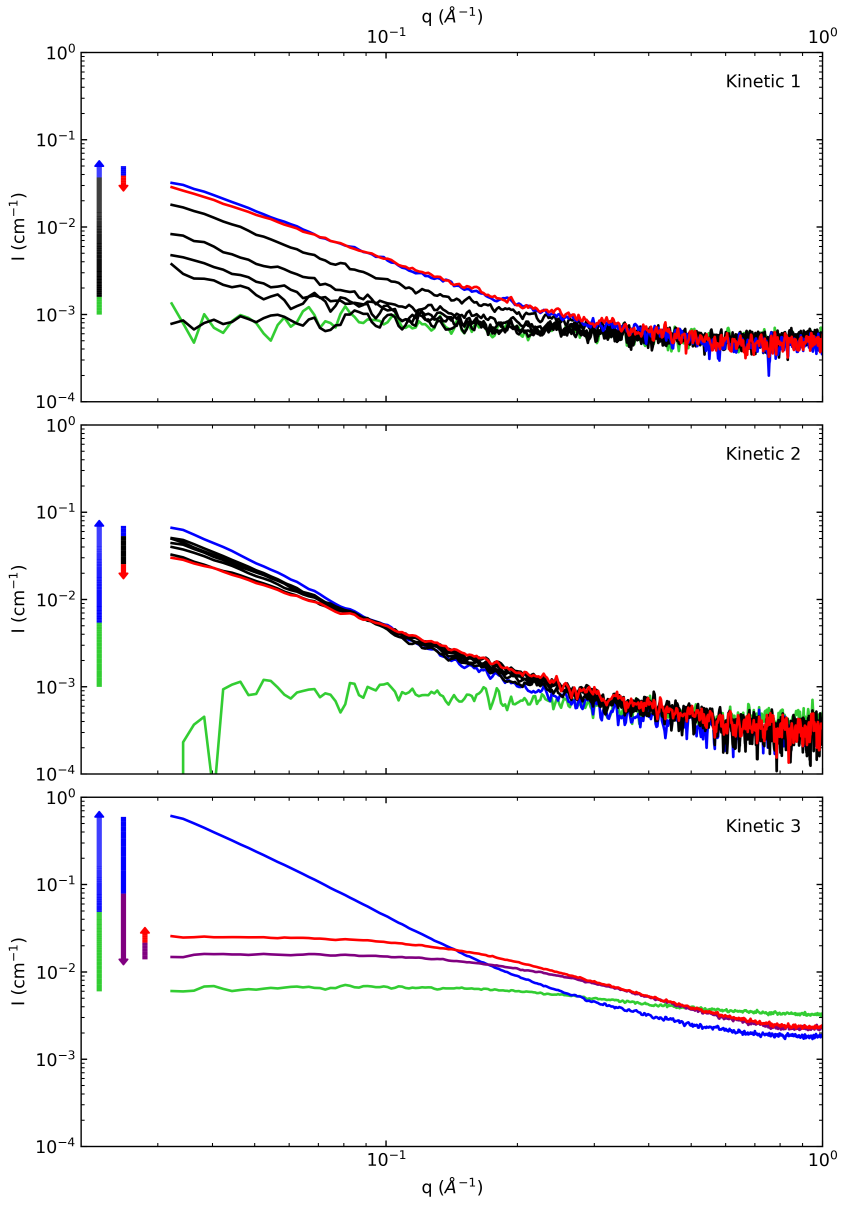

Figure 2: Scattered intensity at different time intervals for the three kinetic experiments. The first intensity and last intensity measured are respectively in green and red, intermediates ones are in black (for kinetics 1 and 2). Purple curve for kinetic 3 corresponds to scattered intensity at 38 min (when I_{qmin} (see text) reaches a minimum value after NaOH injection). Colorful arrows indicate in which directions scattered intensity curves evolve with reaction time.

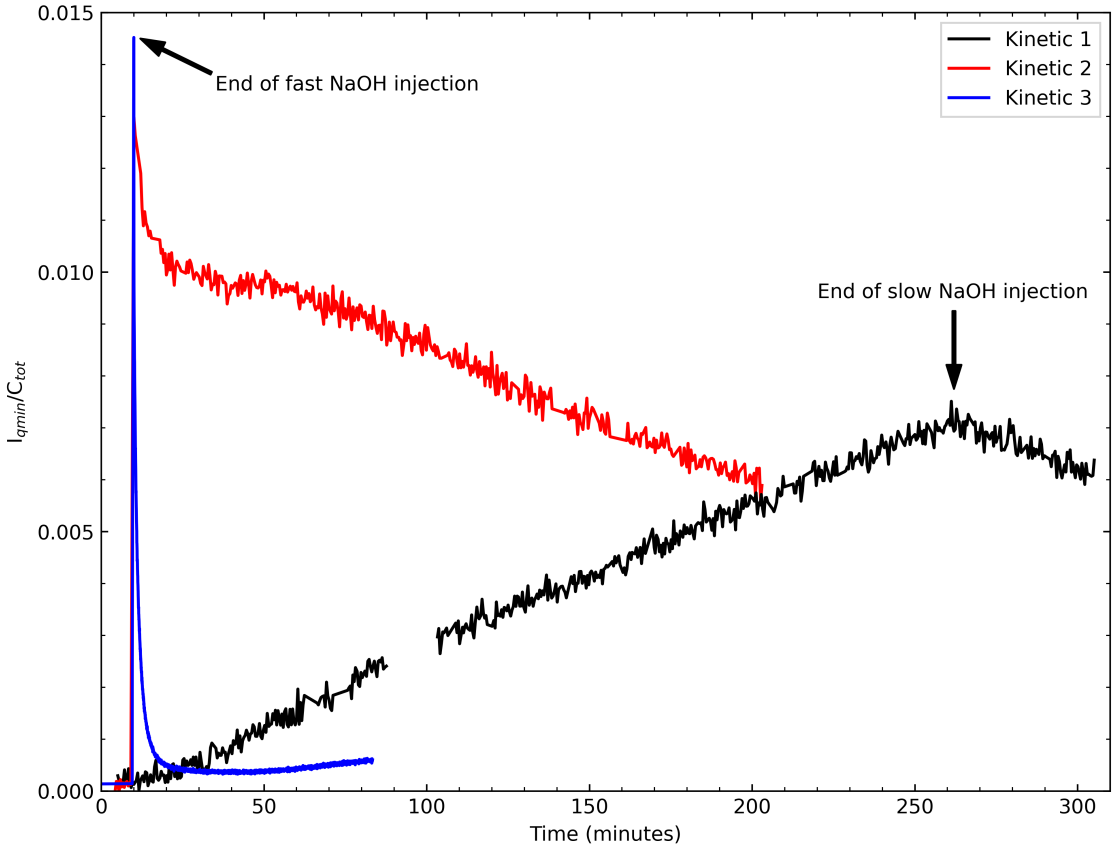

Figure 3: Evolution of I_{qmin}/C_{tot} as a function of time. Injection of NaOH starts at 10 minutes for the three kinetics.

Raman measurement at millimolar concentration is not meaningful because the concentration is too low to be detected. In the case of kinetic 3 however, it is possible to follow the hydrolysis of TEOS with time. Figure 4A shows Raman spectra at various times after TEOS injection of kinetic 3. At centimolar concentration, it is possible to follow the hydrolysis of TEOS that is injected 5 minutes before the NaOH solution. Indeed, when ethanol is released in solution, a peak is observed at 880 cm^{-1} (black arrow) [33, 34]. In order to follow this hydrolysis, we calculate the area of this peak that is displayed in Figure 4B. The peak area of ethanol starts to exceed the background signal at 40 minutes (*i.e.* 35 minutes after TEOS injection) and its intensity continues to increase during the whole experiment. Therefore, depolymerization of *Al* occurs without a measurable signal of hydrolyzed *Si*. As the signal increases at least up to four times the background level, it means that less than 25% of TEOS has been hydrolyzed during the restructuring of the large *Al* polycations. It is also interesting to note that no peak

at 695 cm^{-1} (gray arrow) is observed. This peak is characteristic of silicon condensation, *i.e.* the formation of $Si-O-Si$ bonds [35]. It suggests that when TEOS starts to be hydrolyzed, Si reacts first with the Al polycations and is not involved in a measurable self-condensation. The increase in size of the proto-imogolites between 38 minutes to the end of the experiments at 83 minutes and after an aging period of 10 hours may be driven by the slow continuous release of $Si(OH)_4$ during this period of time. For millimolar concentrations, it can be expected that the hydrolysis reactions occurred much faster due to the higher water to TEOS ratio. In such a case, the $Si(OH)_4$ species are available to interact with Al polycations earlier in the reaction. In this case, the depolymerization is slower than in the case of kinetic 3. The presence of Si from hydrolyzed TEOS seems to slow down the depolymerization of HA polycations.

Figure 5 compares the scattered intensity of the open-ILS prepared in the three different conditions at the end of aging period of 1 day for the millimolar conditions and 10 hours for the centimolar condition. In millimolar conditions, proto-imogolites have almost exactly the same scattering pattern at the end of aging time no matter the speed of NaOH injection. However, they have followed a very different formation mechanism. At slow NaOH injection rate, the condensation of Al is slowly driven by injection of HO^- in a continuous and progressive way. At large injection rate, concentration gradient effects have led initially to a local over-condensation of Al polycations [36, 37]. As soon as NaOH injection stops, the large obtained polycations are restructured and their average size decreases. A pH decrease is also noticed, which tends to prove that this depolymerization goes along with hydrolysis of $Al-OH-Al$ bonds. As already discussed, the presence of Si during the depolymerization of Al polycations in kinetic 2 enables reaching a larger final size than kinetic 3.

In order to obtain a characteristic size of the nano-objects in the dispersion, we calculate a gyration radius R_g using the following approximation (Guinier regime):

$$I(q) \approx I_{qmin} e^{\frac{-(R_g * q)^2}{3}} \quad (1)$$

This approximation holds as q approaches 0 with $qR_g << 1$. The proto-imogolites obtained during kinetic 3 with fast injection are obtained from the depolymerization of initial precipitate of larger size in absence of Si. The final scattered intensity of the polycations appears to be smaller than the one obtained at the end of aging for kinetic 1 and 2. After an aging period of 10 hours, we obtain a gyration radius of $R_g = 10$ Å. Thill et *al.*, using simplified mechanical models, evidenced that the shape of open-ILS depends on their characteristic size [28]. It exists a threshold size for which: i) if open-ILS are smaller they have a spherical shape and ii) if they are bigger they have a tubular shape. This sphere/tube transition threshold occurs at about 30 Å, *i.e.* three times greater than the size of

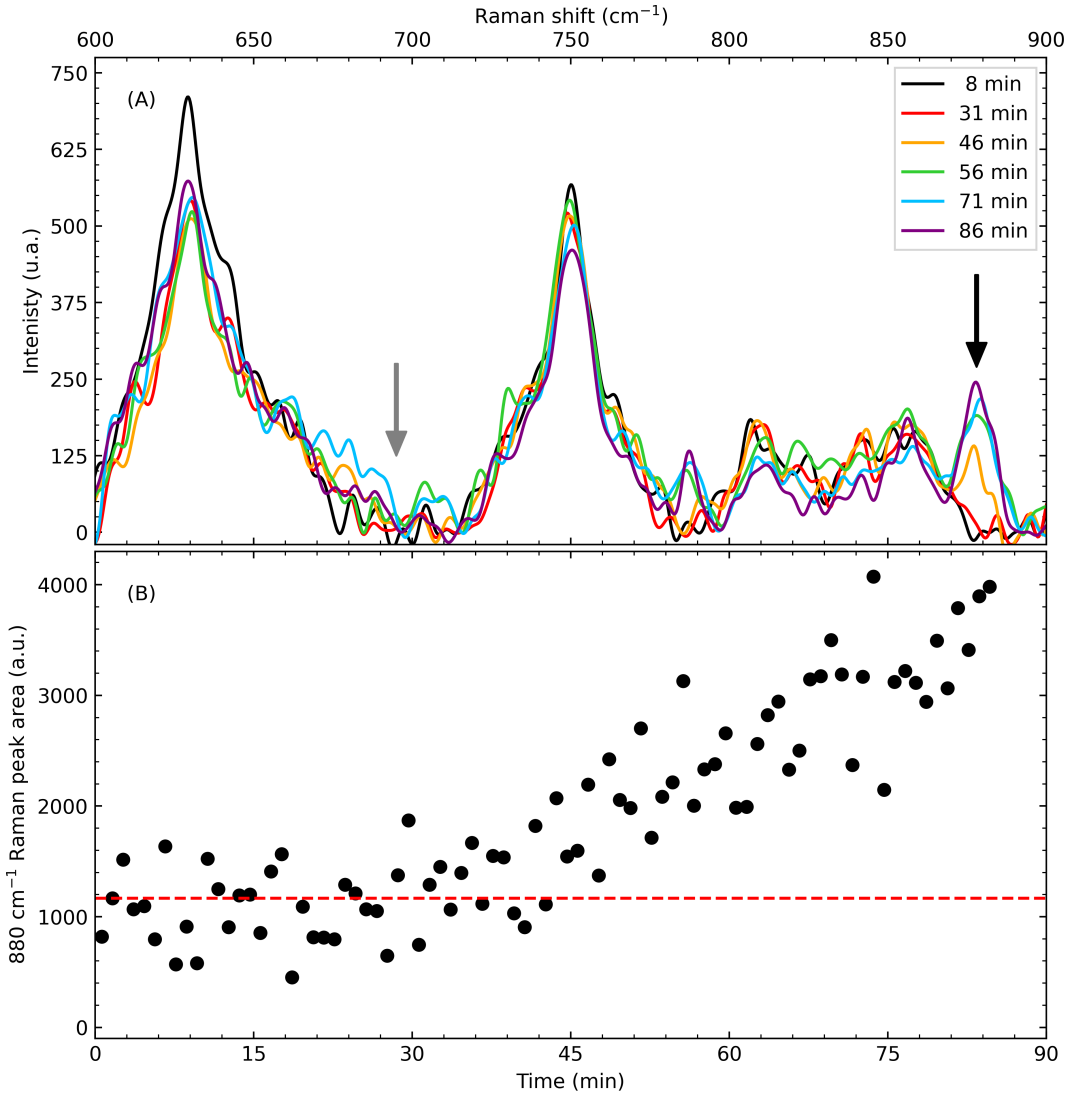

Figure 4: *A*) Evolution of Raman spectrum with time for the centimolar concentration (kinetic 3) and *B*) evolution of the area of pic centered at 880 cm^{-1}. Gray arrow at 695 cm^{-1} and black one 880 cm^{-1} are respectively related to $Si-O-Si$ bond and ethanol.

proto-imogolite for kinetic 3. Scattered intensities of kinetics 1 and 2 have not been measured at low enough angles to reach the Guinier regime. But the I_{qmin}/C_{tot} of the proto-imogolite after 24 hours of aging for kinetics 1 and 2 is about three times higher than kinetic 3. Molecular models of open-ILS, already described by

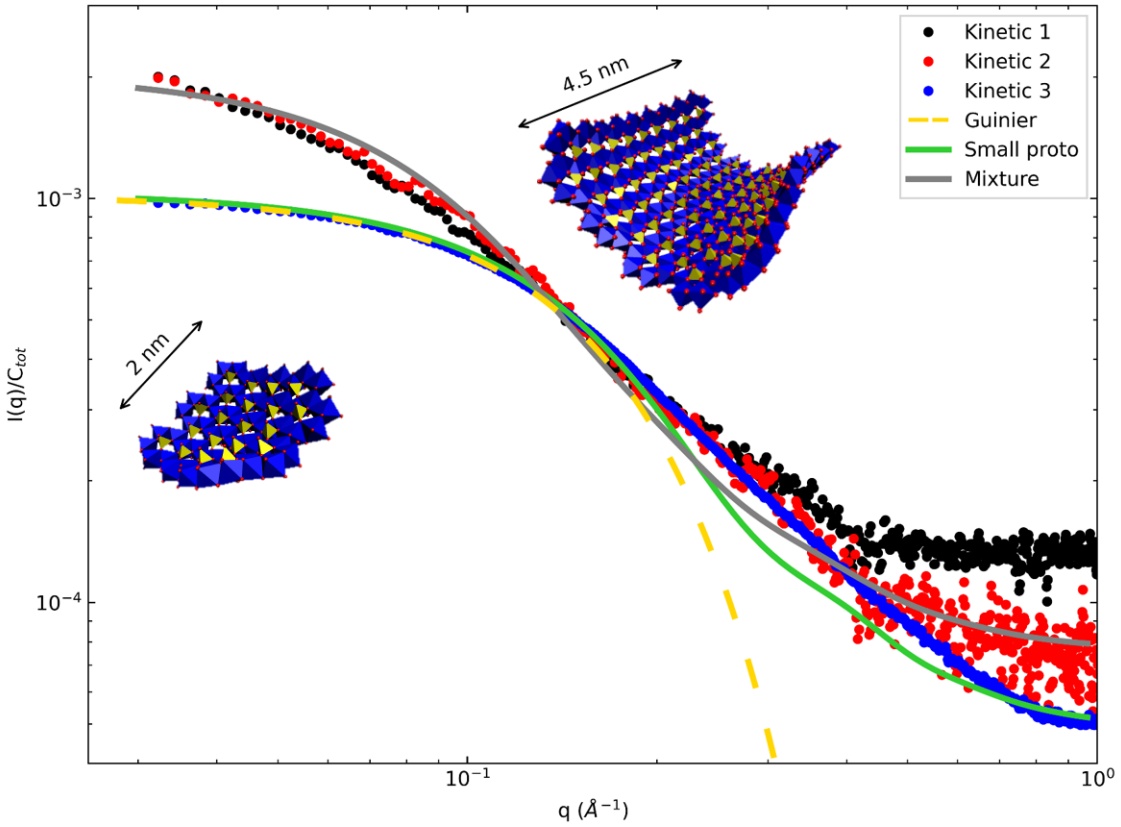

Figure 5: Comparison of the scattered intensities normalized by the concentration for three different conditions after an aging period of 1 day for both millimolar concentrations (kinetics 1 and 2) and 10 hours for the centimolar concentration (kinetic 3). The dotted yellow line is a fit of the Guinier regime for kinetic 3 with $I_{qmin} = 0.001\,\mathrm{cm}^{-1}$ and $R_g = 10\,\text{Å}$. Green and gray curves are respectively scattered intensities of small proto-imogolites and a combination of small (25%) and large (75%) proto-imogolites.

Thill et *al.* [6], are used to compute the scattered intensity using the Debye formula. A small open-ILS containing 152 atoms is displayed in Figure 5. Its border has an extended length of 20 Å. The computed scattered intensity of this small proto-imogolite compares well with the final scattered intensity of kinetic 3 (green curve) and is in agreement with the Guinier gyration radius of 10 Å. For kinetics 1 and 2, a larger model of 1092 atoms has to be used. This model has an extended border length of 45 Å. The scattered intensity of this model structure alone does not reproduce the trend of the experimental intensity. However, a mixture of 75% of large proto-imogolites and 25% of small proto-imogolites as depicted in Figure 5

is close to the experimental intensity (gray curve). The simulation of the scattered intensity of imogolite local structure molecular models can reproduce the shape of the scattered intensity. The size of the proto-imogolite is much smaller in the case of high concentration. For low concentration, a polydisperse distribution of proto-imogolite is probable, with the larger ones having a size above the sphere/tube curvature transition proposed by Thill et *al.* [6].

3.3 From open-ILS to closed-ILS

The three open-ILS (proto-imogolite) samples were put, for a growth stage, in an oven at 90°C for 5 days. The final products were dialyzed against MilliQ water and analyzed by IR spectroscopy and SAXS. Figure 6 shows the IR spectrum between 1200 and 350 cm^{-1} of the final dialyzed products for the three kinetic experiments (Table 1). Peaks around 1100 cm^{-1} and 700 cm^{-1} are related to perchlorate anions remaining after dialysis. The two products obtained at small concentration display a characteristic splitting of the $Si-O$ stretching band at 990 and 935 cm^{-1}. This splitting occurs when the SiO_4 tetrahedra is deformed in a tubular structure. Indeed, in this case, the three $Si-O-Al$ bonds are not equivalent and depend on the chirality of the nanotube. Below the sphere/tube transition, the curvature is the same in all directions and thus the $Si-O-Al$ bonds are equivalent and no band splitting occurs. This is the case for kinetic 3 with a single band at 966 cm^{-1}. This absence of band splitting would be logical before the growth stage with a small R_g value below the sphere/tube transition threshold. The fact that no such splitting occurs after the growth stage could be interpreted by the domination of a self-assembly and aggregation mechanism at constant curvature.

Small Angle X-ray Scattering of the three final products has been measured (Figure 7). Both materials issued from kinetics 1 and 2 display a signature of tubular objects that is well described by (14,0) zig-zag or (8,8) armchair nanotubes. On the contrary, the sample corresponding to kinetic 3 does not display clear oscillations characteristic of monodisperse imogolite nanotubes. It does not either correspond to the scattering of a hollow sphere. For the nanotube samples, it is possible to compare the experimental low angle scattering curves with calculations considering a mixture of nanotubes and open-ILS. We use a simple equation $I_{mix} = (\alpha I_{tube} + (1-\alpha) I_{proto}) * K + B_g$, where α controls the mixture of open-ILS and nanotubes, K is a proportionality parameter to adjust the concentration and B_g is the background scattering. Taking into account the mass difference between the nanotube and the open-ILS, the weight fraction of proto-imogolite is directly proportional to α. An adjustment of the model to the experimental data enables the estimation of this mass fraction. For kinetic 1, we find a weight fraction of large proto-imogolite of 9%. For kinetic 2, the proportion increased to 20%. The

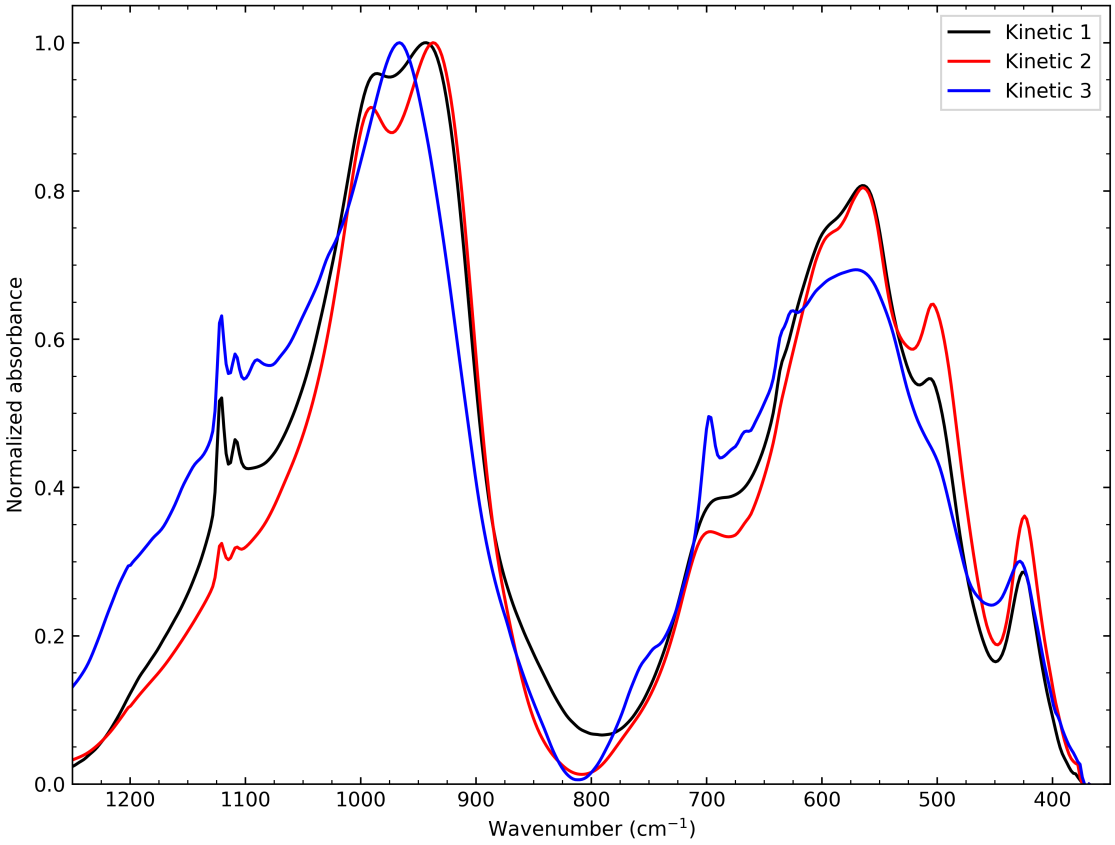

Figure 6: IR spectrum of the final states for the three kinetic experiments.

higher proportion of open-ILS has a damping effect on the oscillations of the scattered intensity of the nanotubes. Interestingly, the IR spectrum shows an increased splitting of the $Si-O$ stretching band for kinetic 2. The open-ILS considered in the SAXS adjustment is above the sphere/tube transition and therefore may also contribute to the splitting of the stretching band. These results show that after dialysis, nanotubes (or nanospheres) coexist with non-tubular nanostructures. We have used open-ILS structures to assess their quantity. We can assess that these nanostructures are the results of closing open-ILSs into less well-defined nanostructures that are not involved in further growth. With the strong approximation that open-ILS can describe correctly the scattering of those closed-ILS, their proportion can be estimated by SAXS.

In the following, we show that it is possible to eliminate part of the non-tubular closed-ILS in a poor imogolite synthesis using a large pore dialysis step. A sample containing more non-tubular nanostructures after the growth stage has been

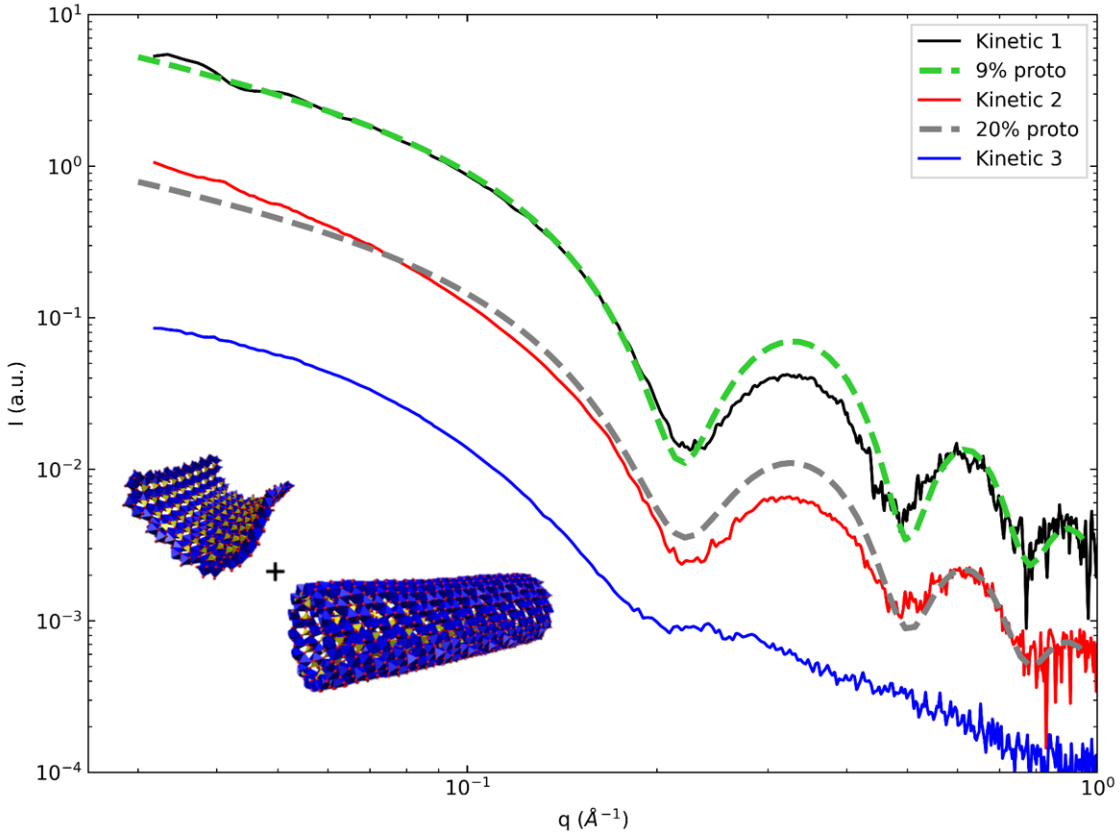

Figure 7: SAXS curves measured after the growth stage for the three kinetic experiments. Molecular structures used to compute the nanotube and large proto-imogolite scattering are also displayed.

obtained by replacing $Al(ClO_4)_3$ with $AlCl_3$ for the aluminum precursor. Figure 8 displays the SAXS curves after a growth stage at 90°C for 5 days and dialysis against MilliQ water for two cut-off sizes: 8 kDa (black curve) and 100 kDa (red curve). The intensity of the first minimum around 0.2 Å^{-1} significantly decreases in the case of the larger pore size dialysis. Using the previous equation, we obtain a weight fraction of proto-imogolite of 50% for 8 kDa and 25% for 100 kDa. Figure S2 shows cryo-TEM images of the corresponding samples (top 8 kDa and bottom 100 kDa). At the 8 kDa cut-off, proto-imogolites are mainly isolated with a characteristic size below 5 nm whereas at the 100 kDa cut-off, no-isolated proto-imogolites are visible. On the contrary, they form aggregates of few tens of nanometers. No such aggregates seems to exist in the sample dialyzed at 8 kDa. SAXS enables a rough estimation of the weight fraction of non-tubular closed-ILS remaining in the dispersion after the growth stage. The shape of the $Si-O$ stretching band in IR

could be envisaged for a similar quantification. However, it seems more delicate than SAXS to interpret as part of the non-tubular closed-ILS can be larger than the sphere/tube transition threshold and thus contribute together with nanotubes to the splitting of the $Si-O$ stretching band. Moreover, with this technique, it is also tough to compare synthesis obtained with different aluminum salts due to remaining anions that are infra-red active in this area (*i.e.* perchlorate anions) and could contribute to the splitting. Through this example, we show that it is possible to reduce the global proportion of non-tubular closed-ILS while maintaining the nanotube dispersion. However, for the moment, no method seems to be available to thoroughly remove non-tubular closed-ILSs while completely preserving both the integrity of the nanotubes and their dispersion state.

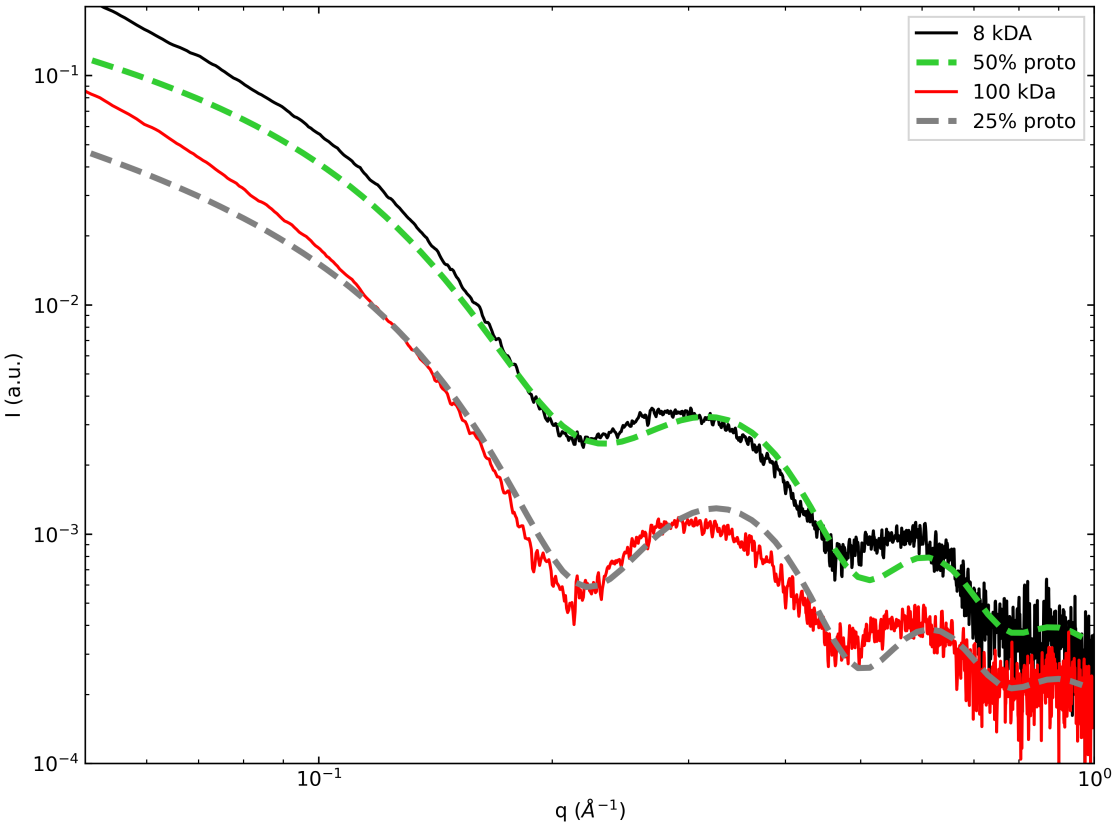

Figure 8: SAXS curves of an imogolite synthesis dialyzed with an 8 kDa (red) and an 100 kDa (black) cut-off.

4 Conclusion and outlook

We have followed the early stages of the formation of hydroxyaluminosilicate nanostructures in an acidic environment and at a Si/Al ratio of 0.55 by synchrotron SAXS and Raman spectroscopy. Our results clearly confirm the important role of open-ILS (proto-imogolites) in the formation of nanostructured species (imogolite, allophane). The concentration and kinetics of TEOS hydrolysis with respect the formation and restructuring of Al polycations appear to be particularly important in the control of the average size of open-ILS. With typical synthesis conditions, this size can span both below (high concentration) and above (low concentration) the sphere/tube curvature transition that occurs at about 30 Å. Moreover, the rate of NaOH injection seems to be less important at least so long as a sufficient equilibration time (several hours) is allowed for the structure of open-ILS to stabilize at ambient temperature. The fact that no splitting of the stretching band of $Si-O$ is observed in the IR spectra at high concentration is in favor of a self-assembly/aggregation mechanism of small proto-imogolites at constant curvature rather than a further growth of the open-ILS upon heating. The precise role of concentration, counter-ions, type of solvent and temperature in the control of the self-assembly of open-ILS has still been barely explored. These results call for further research in this direction in particular for better control of imogolite chirality, length and purity. Finally, while it is possible to reduce the concentration of non-tubular closed-ILS to a few percent in mass, no perfect method was found yet to fully remove them without compromising the dispersion and/or chemical integrity of the nanotubes.

Conflicts of interest

There are no conflicts to declare.

Acknowledgements

The SWAXSlab plateform of NIMBE and LLB is acknowledged for the SAXS facility. We want to thank O. Taché for his help for the SAXS experiments in the SWAXS Lab. (Cryo-)TEM observations were made, thanks to "Investissements d'Avenir" LabEx PALM (ANR-10-LABX-0039-PALM). This work was also funded by the ANR grant BENALOR (ANR-20-CE09-0029). Sophie Charton is acknowledged for her collaboration on this project and for her work with Tobias Lange in Marcoule. Thibault Coradin is acknowledged for his help in supervising the work of Pierre Picot at the time of his PhD during which most experiments presented in this article were performed. The authors thank Dr. Mark Levenstein for reading the manuscript and making insightful comments.

References

[1] C. Levard and I. Basile-Doelsch. Geology and mineralogy of imogolite-type materials. *Developments in Clay Science*, 7:49–65, 2016.

[2] C. Schneider, F. Doucet, S. Strekopytov, and C. Exley. The solubility of an hydroxyaluminosilicate. *Polyhedron*, 23(18):3185–3191, 2004.

[3] C. Exley. Reflections upon and recent insight into the mechanism of formation of hydroxyaluminosilicates and the therapeutic potential of silicic acid. *Coordination Chemistry Reviews*, 256(1-2):82–88, 2012.

[4] P.F. Barron, M.A. Wilson, A.S. Campbell, and R.L. Frost. Detection of imogolite in soils using solid state 29si nmr. *Nature*, 299(5884):616–618, 1982.

[5] G.I. Yucelen, R.P. Choudhury, A. Vyalikh, U. Scheler, H.W. Beckham, and S. Nair. Formation of single-walled aluminosilicate nanotubes from molecular precursors and curved nanoscale intermediates. *Journal of the American Chemical Society*, 133(14):5397–5412, 2011.

[6] A. Thill. *Nanozised tubular clay minerals; halloysite and imogolite*, volume 7 of *Developments in Clay Science*, chapter From molecular precursor to imogolite nanotubes, pages 429–457. Elsevier, 2016.

[7] J. Beardmore, X. Lopez, J.I. Mujika, and C. Exley. What is the mechanism of formation of hydroxyaluminosilicates? *Scientific Reports*, 6, 2016.

[8] V.C. Farmer, A.R. Fraser, and J.M. Tait. Characterization of the chemical structures of natural and synthetic aluminosilicate gels and sols by infrared spectroscopy. *Geochimica et Cosmochimica Acta*, 43(9):1417–1420, 1979.

[9] K.R. Lenhardt, H. Breitzke, G. Buntkowsky, E. Reimhult, M. Willinger, and T. Rennert. Synthesis of short-range ordered aluminosilicates at ambient conditions. *Scientific Reports*, 11(1), 2021.

[10] S. Mukherjee, V.M. Bartlow, and S. Nair. Phenomenology of the growth of single-walled aluminosilicate and aluminogermanate nanotubes of precise dimensions. *Chemistry of Materials*, 17(20):4900–4909, 2005.

[11] C. Levard, J. Rose, A. Thill, A. Masion, E. Doelsch, P. Maillet, O. Spalla, L. Olivi, A. Cognigni, F. Ziarelli, and J.-Y. Bottero. Formation and growth mechanisms of imogolite-like aluminogermanate nanotubes. *Chemistry of Materials*, 22(8):2466–2473, 2010.

[12] C. Levard, J. Rose, A. Masion, E. Doelsch, D. Borschneck, L. Olivi, C. Dominici, O. Grauby, J.C. Woicik, and J.-Y. Bottero. Synthesis of large quantities of single-walled aluminogermanate nanotube. *Journal of the American Chemical Society*, 130(18):5862–5863, 2008.

[13] A. Thill, P. Maillet, B. Guiose, O. Spalla, L. Belloni, P. Chaurand, M. Auffan, L. Olivi, and J. Rose. Physico-chemical control over the single- or double-wall structure of aluminogermanate imogolite-like nanotubes. *Journal of the American Chemical Society*, 134(8):3780–3786, 2012.

[14] G.I. Yucelen, D.-Y. Kang, R.C. Guerrero-Ferreira, E.R. Wright, H.W. Beckham, and S. Nair. Shaping single-walled metal oxide nanotubes from precursors of controlled curvature. *Nano Letters*, 12(2):827–832, 2012.

[15] P. Maillet, C. Levard, O. Spalla, A. Masion, J. Rose, and A. Thill. Growth kinetic of single and double-walled aluminogermanate imogolite-like nanotubes: An experimental and modeling approach. *Physical Chemistry Chemical Physics*, 13(7):2682–2689, 2011.

[16] G.I. Yucelen, D.-Y. Kang, I. Schmidt-Krey, H.W. Beckham, and S. Nair. A generalized kinetic model for the formation and growth of single-walled metal oxide nanotubes. *Chemical Engineering Science*, 90:200–212, 2013.

[17] V.C. Farmer, M.J. Adams, A.R. Fraser, and F. Palmieri. Synthetic imogolite: properties, synthesis, and possible applications. *Clay Minerals*, 18(4):459–472, 1983.

[18] L.A. Bursill, J.L. Peng, and L.N. Bourgeois. Imogolite: An aluminosilicate nanotube material. *Philosophical Magazine A: Physics of Condensed Matter, Structure, Defects and Mechanical Properties*, 80(1):105–117, 2000.

[19] M.A. Wilson, G.S.H. Lee, and R.C. Taylor. Tetrahedral rehydration during imogolite formation. *Journal of Non-Crystalline Solids*, 296(3):172–181, 2001.

[20] P. Du, P. Yuan, A. Thill, F. Annabi-Bergaya, D. Liu, and S. Wang. Insights into the formation mechanism of imogolite from a full-range observation of its sol-gel growth. *Applied Clay Science*, 150:115–124, 2017.

[21] L. Belloni and A. Thill. *Why a 1:1 2D structure tend to roll? A thermodynalic perspective.*, volume 7 of *Developments in Clay Science*, chapter From molecular precursor to imogolite nanotubes, pages 361–386. Elsevier, 2016.

[22] G. Monet, M.S. Amara, S. Rouzière, E. Paineau, Z. Chai, J.D. Elliott, E. Poli, L.-M. Liu, G. Teobaldi, and P. Launois. Structural resolution of inorganic nanotubes with complex stoichiometry. *Nature Communications*, 9(1), 2018.

[23] K. Wada, N. Yoshinage, H. Yotsumoto, and K.I.S. Aida. High resolution electron micrographs of imogolite. *Clay Minerals*, 8:487–489, 1970.

[24] G.H. Koenderink, S.G.J.M. Kluijtmans, and A.P. Philipse. On the synthesis of colloidal imogolite fibers. *Journal of Colloid and Interface Science*, 216(2):429–431, 1999.

[25] Shin-ichiro Wada. Imogolite synthesis at 25 degree c. *Clays and Clay Minerals*, 35(5):379–384, 1987.

[26] C.-Y. Su, A.-C. Yang, J.-S. Jiang, Z.-H. Yang, Y.-S. Huang, D.-Y. Kang, and C.-C. Hua. Properties of single-walled aluminosilicate nanotube/poly(vinyl alcohol) aqueous dispersions. *Journal of Physical Chemistry B*, 122(1):380–391, 2018.

[27] V.C. Farmer, A.R. Fraser, and J.M. Tait. Synthesis of imogolite: A tubular aluminium silicate polymer. *Journal of the Chemical Society, Chemical Communications*, 13:462–463, 1977.

[28] A. Thill, P. Picot, and L. Belloni. A mechanism for the sphere/tube shape transition of nanoparticles with an imogolite local structure (imogolite and allophane). *Applied Clay Science*, 141:308–315, 2017.

[29] Peixin Du, Shun Wang, Peng Yuan, Jiacheng Liu, Dong Liu, Haozhe Guo, Xinyi Xiang, and Xiaolong Guo. Structure of allophanes with varied si/al molar ratios and implications to their differentiation on mars. *Icarus*, 382, 2022.

[30] N. Arancibia-Miranda, M. Escudey, M. Molina, and M.T. García-González. Use of isoelectric point and ph to evaluate the synthesis of a nanotubular aluminosilicate. *Journal of Non-Crystalline Solids*, 357(7):1750–1756, 2011.

[31] P. Maillet, C. Levard, E. Larquet, C. Mariet, O. Spalla, N. Menguy, A. Masion, E. Doelsch, J. Rose, and A. Thill. Evidence of double-walled al-ge imogolite-like nanotubes. a cryo-tem and saxs investigation. *Journal of the American Chemical Society*, 132(4):1208+, 2010.

[32] E. Paineau, M.-E.M. Krapf, M.-S. Amara, N.V. Matskova, I. Dozov, S. Rouzière, A. Thill, P. Launois, and P. Davidson. A liquid-crystalline hexagonal columnar phase in highly-dilute suspensions of imogolite nanotubes. *Nature Communications*, 7, 2016.

[33] J. Gnado, P. Dhamelincourt, C. Pélégris, M. Traisnel, and A. Le Maguer Mayot. Raman spectra of oligomeric species obtained by tetraethoxysilane hydrolysis-polycondensation process. *Journal of Non-Crystalline Solids*, 208(3):247 – 258, 1996.

[34] I.-G. Marino, P. P. Lottici, D. Bersani, R. Raschellà, A. Lorenzi, and A. Montenero. Micro-raman monitoring of solvent-free teos hydrolysis. *Journal of Non-Crystalline Solids*, 351(6-7):495 – 498, 2005.

[35] A. Le Cleach and P. Gillet. Ir and raman spectroscopic study of natural lawsonite. *European Journal of Mineralogy*, 2(1):43 – 53, 1990.

[36] P. H. Hsu. Mechanisms of gibbsite crystallization from partially neutralized aluminum chlorure solutions. *Clays and Clay Minerals*, 36(1):25–30, 1988.

[37] S. Bi, C. Wang, Q. Cao, and C. Zhang. Studies on the mechanism of hydrolysis and polymerization of aluminum salts in aqueous solution: Correlations between the "core-links" model and "cage-like" keggin-al13 model. *Coordination Chemistry Reviews*, 248(5-6):441–455, 2004.

Evidence and importance of intermediate nanostructures in the journey from molecular precursors to allophane and imogolite nanocrystals.

Pierre Picot[a],Tobias Lange[a,b],Fabienne Testard[a], Frederic Gobeaux[a], Sophie Charton[b] and Antoine Thill[a,*]

[a] Université Paris-Saclay, CEA, CNRS, NIMBE, 91191 Gif-sur-Yvette, France.
[b] CEA, DES, ISEC, DMRC, Univ. Montpellier, Marcoule, France.

April 24, 2023

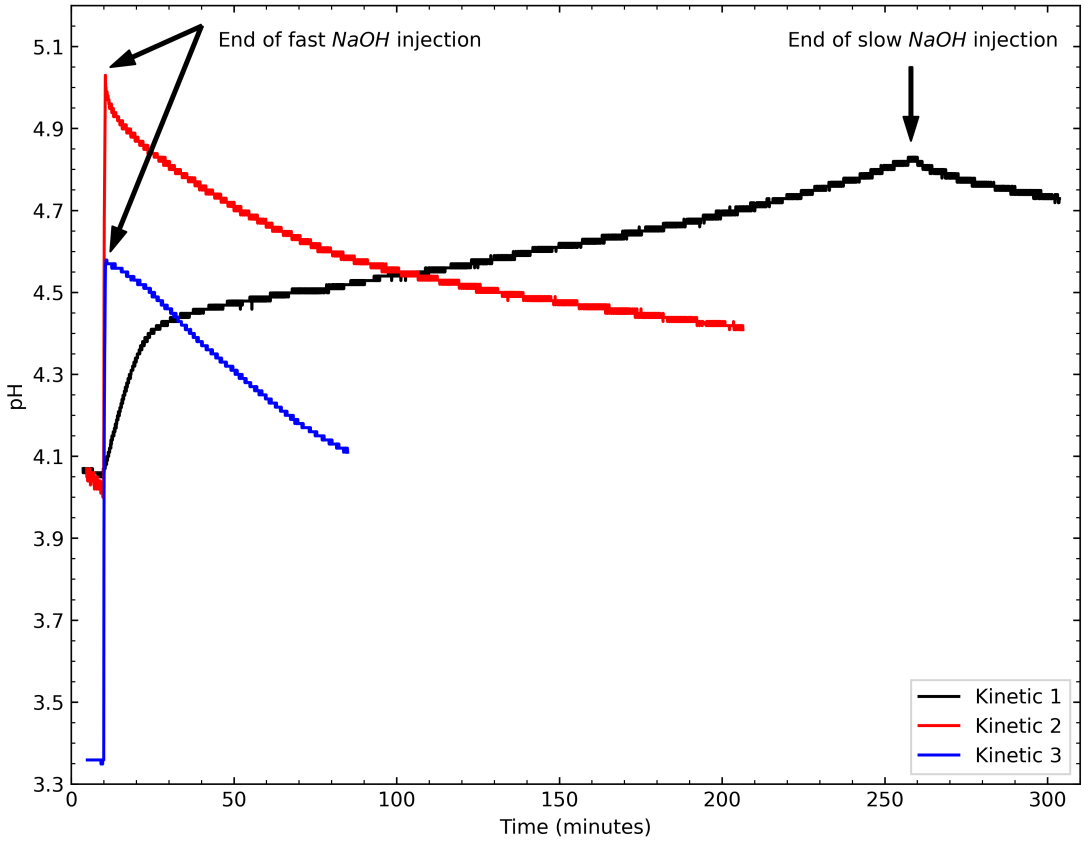

Figure S1: Evolution of pH as a function of time. Injection of NaOH starts at 10 minutes for the three kinetics.

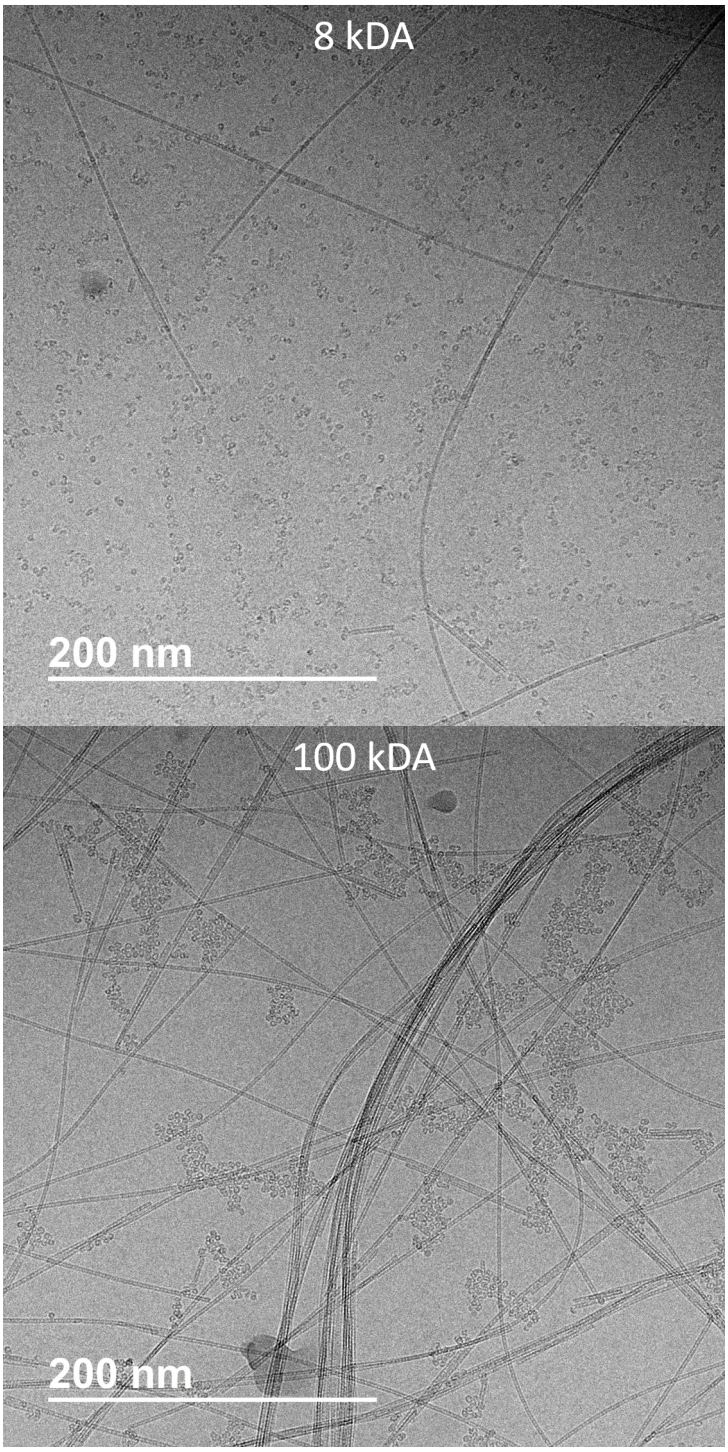

Figure S2: Cryo-TEM pictures of an imogolite synthesis after dialysis: top at 8 kDa cut-off and bottom at 100 kDa cut-off.